Reconstructing 3100 years of extreme coastal flooding events from Emau Island, Vanuatu☆

Yanan Li [a,b,**] , Jeffrey P. Donnelly [b], Shu Gao [a,*], Jianhua Gao [a], James F. Bramante [b], Krishna K. Kotra [c]

[a] Ministry of Education Key Laboratory for Coast and Island Development, School of Geography and Ocean Science, Nanjing University, Nanjing, China
[b] Coastal Systems Group, Department of Geology and Geophysics, Woods Hole Oceanographic Institution, Woods Hole, MA, USA
[c] School of Agriculture, Geography, Environment, Ocean and Natural Sciences, The University of the South Pacific, Emalus Campus, Port Vila, Vanuatu

ARTICLE INFO

ABSTRACT

Tropical cyclones (TCs) are posing growing threat to coastal populations and property, thereby necessitating more millennial paleoclimatic reconstructions. This study presents a 3100-year record from Marou Lagoon, Emau Island, Vanuatu. Using coarse anomalies as the main proxy, 36 intense tropical cyclones are identified (~1.2/century). Active TC phases occurred during 1550–1750 CE, 350–750 CE, and the 20th century, contrasting with a pre-Common Era quiescent period. Comparative analysis with five paleotempestological records across the tropical South Pacific reveals multidecadal-to-centennial TC variability is dominantly governed by ENSO-driven shifts in the South Pacific Convergence Zone (SPCZ). La Niña-like periods cause southwestward SPCZ displacement and expansion, causing basin-wide enhanced cyclogenesis, while persistent strong El Niño conditions collapse the SPCZ into a zonal structure near French Polynesia, concentrating activity at eastern sites and suppressing western ones. Weak-to-moderate El Niño states exhibit stochastic dominance. Critically, sedimentological analysis reveals the most prominent event bed represents the cataclysmic Kuwae eruption in mid-15th. This deposit exhibits a five-stage sequence reflecting eruption progression, providing unprecedented resolution of eruption dynamics and tsunami impacts that surpass subaerial records. Typical diagnostic features of tsunami deposits (e.g., hummocky cross-stratification) are absent due to lagoon barrier/reef sheltering, and the heterogeneous density and shape of dominant pyroclastic materials (especially pumice) invalidate standard hydraulic grain-size models. This study demonstrates that sheltered lagoons preserve high-fidelity records of both extreme TCs and volcanogenic tsunamis. Such archives offer critical insights into regional climatic drivers and geohazard mechanisms but require environment-specific sedimentological frameworks, particularly where low-density pyroclastics dominate coarse fractions.

1. Introduction

Tropical cyclones (TCs) pose an increasing threat to coastal populations and infrastructure, highlighting the critical need to understand how climate change influences TC activity on decadal to centennial timescales. Such insights are essential for assessing future risks to coastal communities and infrastructure under evolving climate scenarios.

Beyond the temporal limitations of instrumental records, sedimentary archives provide valuable proxies for reconstructing TC activity on multidecadal to millennial timescales. Extreme TC-driven waves and currents deposit coarse-grained sediments within finer-grained, quiescent-weather deposits, forming distinct "event beds". Coastal lakes, ponds, lagoons, and karst basins are particularly suitable for preserving continuous TC records, as event beds deposited below the wave base are

less susceptible to reworking under normal hydrodynamic conditions. Since the seminal study of Emery (1969), numerous long-term TC reconstructions have been developed along the margins of the western North Atlantic Ocean, the Gulf of Mexico, and the Caribbean Sea (e.g., Liu and Fearn, 2000; Donnelly et al., 2001; Donnelly and Woodruff, 2007; Lane et al., 2011; Brandon et al., 2013; Donnelly et al., 2015; Wallace et al., 2019; Donnelly, 2025) and within the western North Pacific basin (e.g., Liu et al., 2001; Yu et al., 2009; Yue et al., 2019; Bramante et al., 2020; Yang et al., 2022; Tan et al., 2023).

Low-lying island nations in the South Pacific face heightened exposure to TCs (Charan et al., 2017), yet continuous prehistoric TC records from this basin remain sparse. Notable efforts include Toomey et al. (2013), who reconstructed a 5000-year TC record from a back-reef lagoon in Tahaa, French Polynesia and linked active TC periods to insolation variations and the El Niño–Southern Oscillation (ENSO). Denniston et al. (2015) reported a 2200-year record of extreme rainfall events associated with TC activity from an Australian cave, suggesting multi-centennial variations influenced by ENSO. Toomey et al. (2016) presented a 3000-year TC record from Apu Bay, Tahaa, French Polynesia, correlating its centennial to millennial variability with shifts in the South Pacific Convergence Zone (SPCZ). Recently, a millennial-scale sedimentary archive from a coastal sinkhole in Fiji (Li et al., 2025)

emphasized the dominance of SPCZ displacements in characterizing centennial TC variability across the western and central South Pacific.

Sedimentary environments on South Pacific volcanic and coral islands are particularly conducive to multi-centennial and millennial-scale TC reconstructions. Crucially, these islands experience frequent TC activity, ensuring a high recurrence of events capable of generating distinct geological signatures. Furthermore, these islands commonly contain stable coastal embayments, such as lagoons and sheltered bays, which act as natural sediment traps preserving storm deposits with minimal reworking or erosion. Volcanic islands also supply abundant terrigenous sediments, while adjacent coral reefs contribute substantial marine carbonate sediments. This readily available and compositionally distinct sediment supply facilitates the formation of clearly identifiable storm-induced deposits within finer-grained background sediments.

Due to the tectonic setting at the Pacific and Indo-Australian Plate boundary, tsunamis induced by volcanic eruptions and earthquakes also pose substantial risks to South Pacific islands (Goff et al., 2011; Charan et al., 2017). For instance, Vanuatu experiences frequent and intense seismic events originating from the Vanuatu subduction zone (Kruger-Knuepfer et al., 1986). Distinguishing tsunami deposits from TC event beds is essential due to their similarity; physical features, such as coarse grain composition, grain size, grading, thickness and erosive
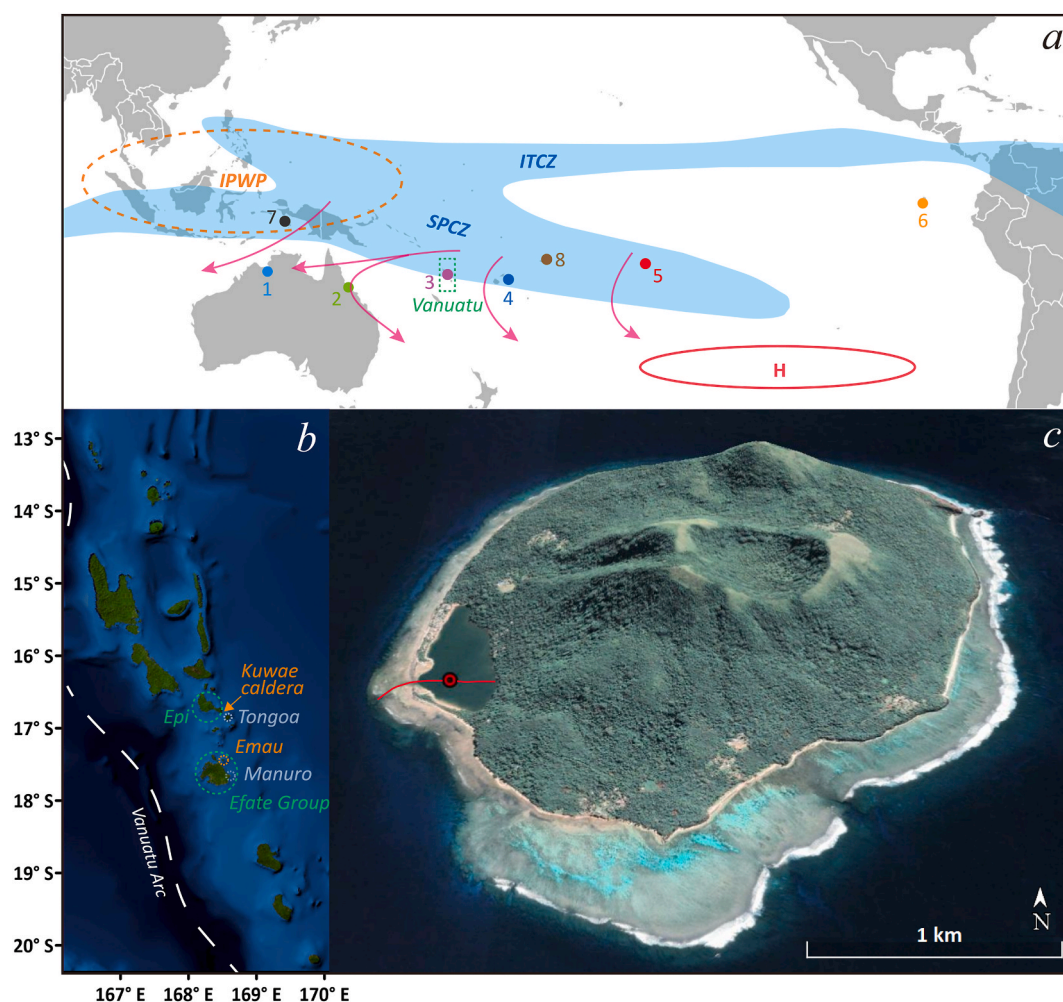
Fig. 1. The study site. (a) A schematic illustrating positions major climate features in the South Pacific basin. The blue-shaded bands show the climatological average positions of the Intertropical Convergence Zone (ITCZ) and the South Pacific Convergence Zone (SPCZ), the orange (dashed) and red oval (with H inside) represent the annual positions of the Indo-Pacific Warm Pool (IPWP) and subtropical South Pacific high during neutral ENSO states, purple arrows indicate different tropical cyclones tracks, numbered dots mark the sites of paleoclimate records in Fig. 5, and the dashed rectangle encloses Vanuatu. (b) An overview of the major islands of Vanuatu. Colored circles envelope the Efate Group, the Island of Emau, Epi, Tongoa, and Manuro beach (Hong et al., 2018), and the arrow indicates the Kuwae caldera (image source: USGS). (c) Topographic image of the Island of Emau; the target mark shows the coring location (17°29′17″ S, 168°28′30″ E, water depth ~9.5 m at the time of coring), and the red line indicates a profiling transection (image source: Google Earth™, 2025).

lower contacts should be comprehensively employed as criteria for differentiation (Spiske et al., 2013; Biguenet et al., 2022); however, the applicability of these approaches can be disputed across different site settings.

Based on a 3100-year sedimentary core from Marou Lagoon on Emau (Emao) Island, Vanuatu, this study aims to address the following key scientific questions: (1) What is the history of intense tropical cyclone activity in the region over the past 3100 years, and how is it linked to the ENSO-SPCZ climate system? (2) How can the deposits of a massive volcanic eruption and its associated tsunami be discriminated and reconstructed at a high resolution from the sedimentary record? (3) How can effective event stratigraphic criteria be established in sheltered, pyroclastic-dominated sedimentary environments?

2. Study site and methodology

2.1. Study site and field methods

The Republic of Vanuatu is an archipelago consisting of several chains of subaerial and submarine volcanic islands along the Vanuatu Arc (Fig. 1a). In the central chain lies the Efate Group, extending back to late Miocene to Holocene (Raos, 2001). The Island of Emau is located to the northeast of the main island Efate, which features a volcanic cone, fringing coral reefs and a lagoon in the west (Fig. 1b); the well-preserved Emau volcano cone (Fig. 1c) is covered with weathered pyroclastic and is heavily vegetated, and is suggested to be much younger than Efate, probably just a few thousand years old (Raos, 2001).

The Vanuatu archipelago typically encounters approximately two TCs annually, most occur from November through April (PACCSAP, 2015). The waves along Efate group coasts are subject to the influence of the southern trade winds and the SPCZ, travelling predominantly from the southeast and south, with a relatively stable height of approximately 1.2 m throughout the year (PACCSAP, 2015). Vanuatu has predominantly semidiurnal tides with a tidal range of approximately 1.2 m (Bureau of MeteorologyAustralia Government, 2024).

The lagoon, covering approximately 0.25 km^2, is separated from the open sea by a barrier, which rises to about 10 m above the mean sea level at its highest point and is abundant with biogenic carbonate sands and gravels. Marou village is located on the barrier and has a population of 300 (Ruehr, 2021). The lagoon (referred to as Marou Lagoon hereinafter) east shore borders the volcano cone (Fig. 1b and c). An inlet cuts through the barrier at the southwest of the lagoon, with a tidal channel extending westward into the coral reef to the open sea. The coral reef flat (~200 m wide) consists of unconsolidated biogenic carbonate sands, shell fragments and rounded volcanic sands.

After mapping the sub-bottom stratigraphy of Marou Lagoon with an Edgetech 3100 Chirp sub-bottom profiling system in November 2017, we collected five incremental core sections using a Livingstone-type drive rod piston corer from a portable raft. The water-sediment surface was recovered and preserved in the top section.

2.2. Sediment analysis

The core sections were transported to the Woods Hole Oceanographic Institution (WHOI) where they were subsampled at contiguous 1 cm intervals, and two subsamples (~1.5 cm^3 each) were extracted from each interval. One subsample was dried at 110 °C overnight to determine its water contents; it was then wet sieved to retain grains coarser than 63 μm, and residuals were dried at 100 °C to determine the coarse fraction (>63 μm). The second subsample was dried at 100 °C overnight and combusted at 550 °C for 1.5 h using the loss-on-ignition method (Dean, 1974) to estimate the organic carbon content. Coarse fraction and organic carbon contents were used to match overlaps between consecutive sections and eliminate redundancies, and the merged single composite continuous core is designated EMAU.

2.3. Event bed identification

Only a few event beds are visually distinct due to their coarse-grain contents and sharp contacts with underlying sediments. More generally, coarse fraction anomalies derived from coarse fraction analysis were employed to delineate coarse deposits downcore. Following the methodology of Donnelly et al. (2015), a coarse fraction cutoff was established to constitute event beds in EMAU. To highlight coarse fraction anomalies, decadal variability was smoothed by subtracting an 11-point moving average baseline, excluding major peaks to avoid overshadowing adjacent minor peaks. The number of event beds identified from coarse fraction anomalies depends on the cutoff threshold applied, determined through sensitivity analysis.

2.4. Age control

Nine terrestrial plant macrofossils were recovered from the core and were radiocarbon dated at the National Ocean Science Accelerator Mass Spectrometer on the WHOI campus. From top surface to 15 cm depth, 9 samples were collected at 1 cm or 5 cm intervals for ^{210}Pb and ^{137}Cs dating. A probabilistic age-depth model for EMAU was derived from part of the radioactive dating results with the Bacon software (v2.3.5) (Blaauw and Christen, 2011). Depth corrections were performed due to the presence of major event beds thicker than 1 cm.

2.5. Event frequency determination

Using the age-depth model and the identified event beds, we constructed a time series and calculated event frequency (events per century) following the method of Lane et al. (2011). A 100-year sliding window was applied to the event data, counting the number of events within each window to estimate their centennial frequency. This approach enables comparison with other centennial-scale event records and paleo-climatological reconstructions.

3. Results

3.1. Coring location and lithofacies of the core

The west-east seismic run (Fig. 1c) indicated that the maximum water depth (~11 m) was near the steep back-barrier side, and the bottom sediment thickness is approximately 15 m (Fig. S1). The location directly facing the inlet was selected as the coring site (Fig. 1), since this area exhibits the greatest sediment thickness and offers the optimal preservation potential of event beds.

EMAU core is approximately 350 cm long (Fig. 2c) and shows various lithofacies. Predominantly the core features dark tan (Munsell color 10 YR 1/2) and dark grey (Munsell color N1) colored fine sediments. Although laminations are indiscernible on visual inspection (Fig. 2b), they are evident on x-ray photographs throughout most of the core (Fig. 2a). The core is punctuated by multiple event beds, which fall into two categories.

3.2. Type-I event bed

The most conspicuous feature of EMAU is an extraordinary event bed (see the green box in Fig. 2a and b; designated as Type-I event bed hereinafter), corresponding to a major coarse fraction peak ranging from 60 % to 95 % (Fig. 2c). This bed consists of several vertical-stacking sublayers (Fig. 3), while no evidence of cross-stratification was observed. Grain sizes of the coarse contents in sublayers range from very fine sand to coarse pebble, and these heterogeneous grains are combinations of various pyroclastic and carbonate bioclastic (Table S1), indicating different sources. The 9 cm thick Sublayer 1 (SL1) is almost entirely composed of well-sorted glassy volcanic ash (MS1; MS means microscope); it was either directly produced by the Emau volcano or was
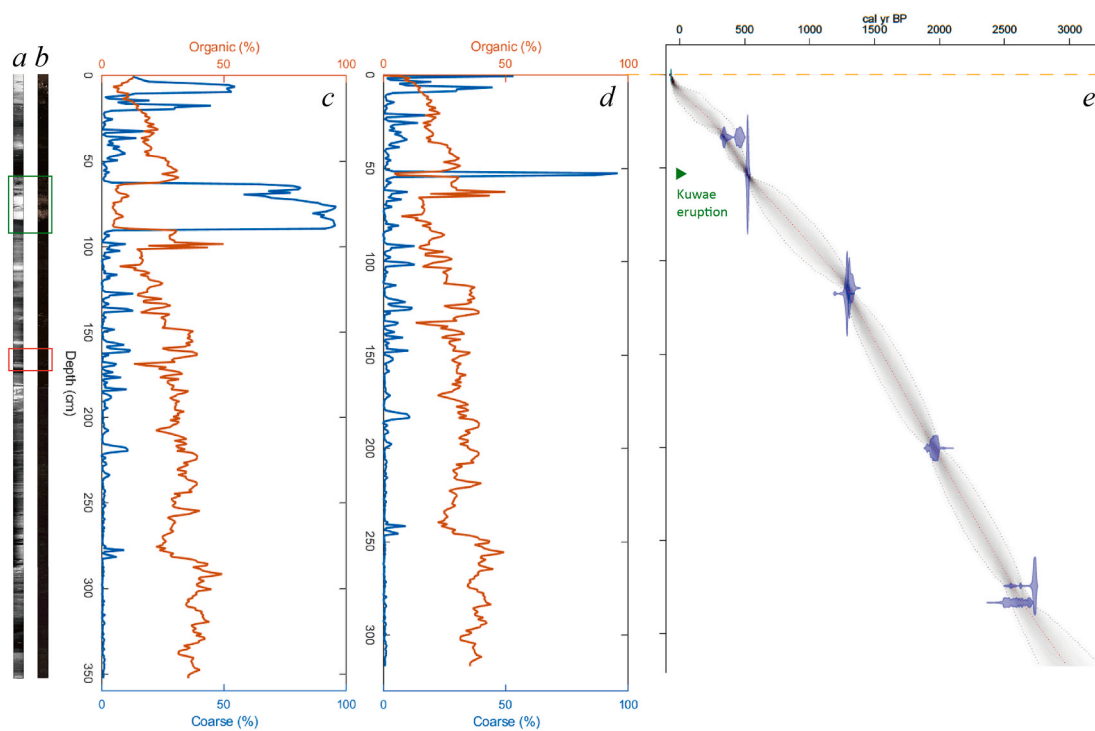
Fig. 2. Overview of the EMAU core. (a) Radiograph and (b) optical graph, (c) original and (d) depth-corrected coarse grain (>63 μm) and organic carbon fractions, and (e) age model. Event beds enclosed within the green and red boxes are described in details in Figs. 3 and 4. Event beds thicker than 1 cm in (c) have been corrected to 1 cm in (d).
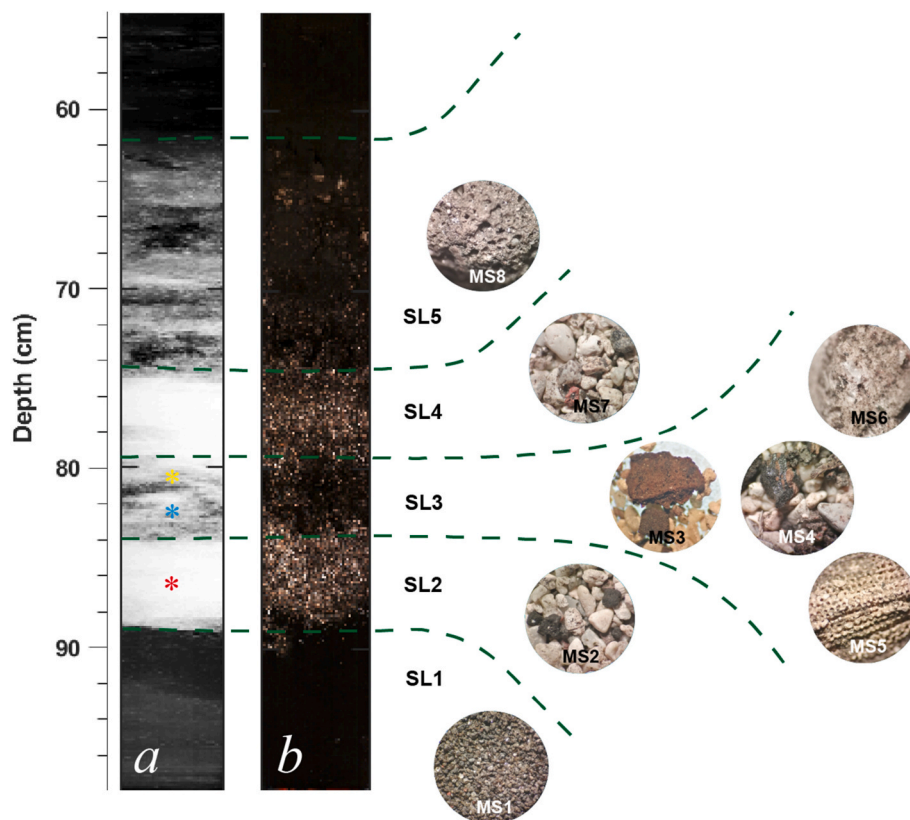
Fig. 3. Details of the Type-I event bed. (a) and (b) are respectively the radiograph and optical graph of the section enclosed with a green box in Fig. 2; MS1 ~ MS8 show the sieving residues coarser than 63 μm under a 40x microscope; colored asterisks mark the depths at which radiocarbon samples were taken.

laterally dispersed by the explosive eruption column from a nearby volcano (e.g., Ambrym, Kuwae, Lopevi, Yasur, etc.). Mixtures of sub-rounded carbonate and volcanic sands (MS2 and MS7) in SL2 and SL4 resemble surface sediments on nearby coral reef flat. Coarse contents in SL3 are complicated: MS4 is essentially the same as MS2 and MS7, while coral fragments (pebble, SL5) are of marine origin, and angular lapillus (SL3) and sub-rounded pumices (SL6) are terrestrial sediments. SL5 is an abrupt blend of pumice gravels and clay; the pumices can be terrestrial, rafted or airborne; the clay color (organic content) shows an upward darkening (increasing) trend.

Three radiocarbon samples were recovered only a few centimeters apart in SL2 and SL3 (Fig. 3); in stark contrast, their dating results are centuries apart (Table S2), suggesting they were transported from different sources and are probably not contemporary with this event. The youngest sample of the three and the one just above the event bed, dating back to 805 yr BP (uncalibrated) and 365 yr BP (both uncalibrated), respectively, provide lower and upper bounds for the causative event.

3.3. Type-II event beds

As shown in Fig. 4, Type-II event beds are a few millimeters to centimeters thick and are usually visually discernible. Light-colored shell fragments and rounded carbonate sands, and dark tan glassy volcanic ash are mixed within dark mud, and there is no evidence of sorting. Coarse contents are like those in surface samples collected from the nearby coral reef flat. The background coarse content is generally lower than 1 %, while coarse fractions in thick beds are over 50 %, and they are only a few percents in thin beds due to the dilution of the sampling interval. The organic carbon fractions range between 5 % and 50 %, and significant negative correlation between the coarse and the organic carbon fractions are only found in major event beds of this type.

4. Discussion

4.1. Tsunami deposit induced by the Kuwae eruption

4.1.1. Kuwae eruption in the Mid-15th

The complex sediment contents and indicated sources, sorting, and cyclic sedimentary structures suggest the Type-I event bed was predominantly produced by a tsunami event. The chronological constraints position the Kuwae eruption in the mid-15th (the Kuwae eruption hereinafter) as the most probable cause of this event bed.

The Kuwae volcano is located about 70 km north of Emau Island

(Fig. 1a), and its eruption in the fifteenth century is regarded as one of the world's most violent volcanic events since the Holocene, and has global weather and climate impacts (Briffa et al., 1998; Gao et al., 2006; Witter and Self, 2007). The eruption commenced with an explosive pre-climatic phase, which likely lasted for months (Witter and Self, 2007); during this juvenile eruption, ash plumes were blasted several kilometers into the atmosphere, followed by massive scoria fall (Woods, 1995). After this stage came the climatic phase, which featured large-scale eruptions of dacite magma and a short-lived sulfur gas release (Witter and Self, 2007). During this period, the successive collapses of the southeastern and northwestern basins formed the enormous submarine Kuwae caldera (12 × 6 km) between Epi and Tongoa islands (Fig. 1b), which remains active to this day (Robin et al., 1994).

4.1.2. Kuwae eruption-triggered tsunami event formation

Generally, diverse tsunamigenic processes are associated with volcanic activity, making it almost the most widely known and common mechanism (only second to seismic activity) generating tsunamis (Day, 2015). Source events involved in an explosive eruption range from submarine volcanic explosions (phreatomagmatic eruption), entry of pyroclastic flows into the ocean, landslides of volcanic materials, ground deformations (e.g., caldera subsidence) and earthquakes (Paris et al., 2014; Day, 2015). Most volcanic tsunami wave trains are dominated by short-period waves, their impacts are therefore restricted to proximal due to the wave dispersion during propagation, and large amplitudes are only observed near source; while those generated by gigantic explosive eruptions with massive lateral landslides and caldera collapses can break out of such wave length and period limitation (Day, 2015; Terry et al., 2022).

Considering the magnitude of Kuwae eruption and its caldera collapse (Witter and Self, 2007), the resultant tsunami waves probably had long periods and basin-wide impacts. However, there are currently few works on paleo-tsunami deposits triggered by the Kuwae eruption except the excavations on the west coast of Efate (Garanger, 1972) and extensive evidence from Epi, Tongoa and Efate group (Goff et al., 2008; see Fig. 1b). Since this tsunami bed has been well preserved deep in the lagoon, it can probably provide more information about the dynamic and material supply variations during different stages of Kuwae event than subaerial deposits.

The formation processes of this bed are inferred according to its sedimentary structures, compositions and known information of Kuwae eruption, as follows: **Stage I**: Ash plumes produced during the pre-climatic eruption of Kuwae were laterally transported downwind for hundreds of kilometers, and the accumulation of glassy ashes
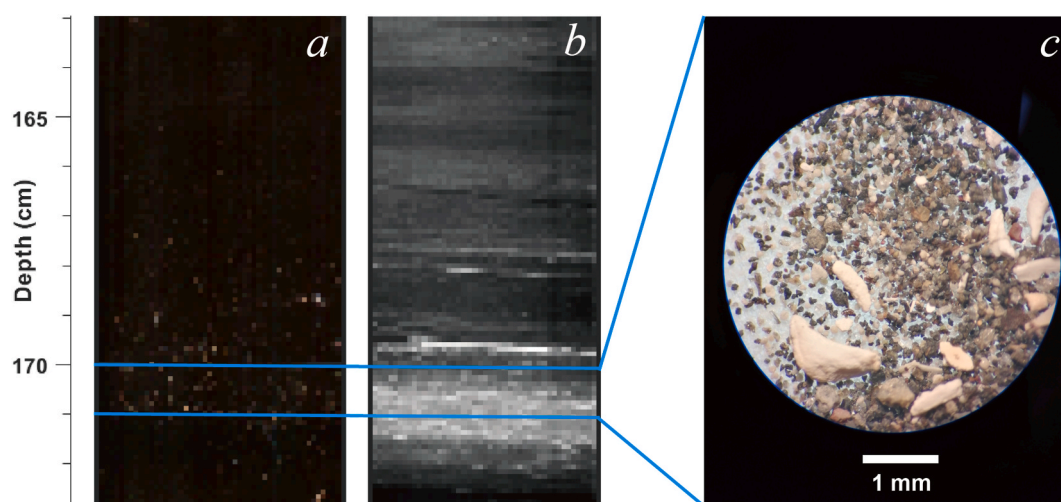
Fig. 4. A typical Type-II event bed. (a) and (b) are respectively the radiograph and optical graph of the section enclosed with a red box in Fig. 2. Between 169.5 cm and 171.5 cm is a typical Type II event bed. (c) shows the sieving residues coarser than 63 μm at 170.5 cm (under a 40x microscope).

constituted sublayer SL1 in Marou Lagoon. Apart from direct scoria fall onto islands adjacent to Kuwae vent, porous scoriae were probably transported by currents and reached farther islands such as Emau. Loose scoria gradually disintegrated due to active dynamics on reef flats and settled down, while pumice rafts could float for months. **Stage II**: During the climatic eruption period, submarine volcanic explosions and pyroclastic flows into the ocean resulted in short-period tsunami waves, which were probably comparative to the combination of storm surges and waves when reaching Emau Island due to dispersion. Unconsolidated carbonate and sand-size pyroclastic particles from the coral reef flat were brought into the lagoon by these moderate waves through the tidal inlet (SL2). **Stage III**: Collapse of the Kuwae vent caused a tremendous tsunami wave train, the highest waves of which ran up and overtopped the cone foot of Emau volcano and the barrier of Marou Lagoon from north. Apart from sand-size carbonate and pyroclastic particles, these gigantic waves scraped coral fragments in deeper parts of the fore reef, coarser pyroclastic on reef flats, and plant debris on the cone surface and dumped them into the lagoon basin (SL3). At the same time, a thick layer of floating pumice poured in and completely covered the lagoon. **Stage IV**: Following the largest waves in the train, subsequent wave magnitudes waned – including those reflected by Efate Island (likely resembling Stage II characteristics) – ultimately depositing the SL4. **Stage V**: It took years for the floating pumice layer to gradually absorb water and settle down (SL5). During this period, the lagoon was almost completely deprived of primary production since sunlight was blocked. As a result, the clay filling in between the pumice rendered lighter color at the bottom of SL5 due to the lack of organic matter, and the recovery of primary production accompanying the fall of pumice induced an upward darkening trend in this sublayer.

Notably, formation of this tsunami event bed spanned several years, during which storm deposits may also be incorporated. However, SL1 and SL5 both exhibit homogeneous compositions with no evidence of storm contributions, although they were deposited over extended periods. SL2–SL4 were formed rapidly and their sieving residues are coarser than those of storm deposits; even if storm sediments were incorporated into these sublayers, such inclusions were probably minimal and indistinguishable.

4.1.3. Peculiar tsunami deposit sequence

The tsunami-induced sublayer sequence (SL2–SL5) notably differs from previous classical models of tsunami depositions due to the sedimentary environments and the nature of coarse sediment. Hummocky cross-stratifications are regarded as indicators of large storm waves and tsunamis (Dott and Bourgeois, 1982; Fujiwara and Kamataki, 2007) and are usually found over sand beds at shallow, wave-dominated, nearshore marine environments. However, the shelter of the barrier and coral reef, and the water depth of Marou Lagoon prevent cross-stratifications from occurring in this event bed. For the same reason, there are no internal structures that indicate repeated turnover of paleocurrents, which have been used for tsunami deposit identification (e.g., Fujino et al., 2006).

Normal and inverse grading are often identified in and between sublayers of tsunami deposits from muddy bay (Fujiwara et al., 2000; Donato et al., 2009; Moreira et al., 2017). It should be emphasized that coarse grains involved in such tsunami deposits are commonly compact silicious particles with similar shapes and densities, which means their grain sizes can be used as proxies to invert dynamic variables such as settling velocity and critical shearing stress, and subsequently to estimate tsunami wave sizes (Jaffe and Gelfenbaum, 2007). However, such implicit conditions are missing from the tsunami bed in EMAU since its coarse compositions have various densities and shapes. Although the medium-coarse-medium trend lying in SL2-SL3-SL4 reflects the dynamic variations of tsunami wave, applying classic empirical models based on siliciclastic to pumice in SL5 would significantly misestimate the sediment dynamic properties of porous pyroclastic (Dioguardi et al., 2018) and lead to wrong conclusions.

Overall, particle size and its derivative concepts such as sorting and grading in tsunami deposits are less informative with heterogeneous lithology. A tsunami model should be constructed with dynamic variables as the kernel, and it must be incorporated with local geological and geographical settings to be more versatile in practical applications, especially in tropical volcano-coral reef environments.

4.1.4. Refining the age-depth model with the Kuwae eruption event

The three samples within the event layer are of exogenous origin, and their dating results (Table S2), with marked dispersion, all predate the tsunami occurrence. Therefore, except that the chronologically youngest specimen among them roughly constrains the lower bound of the event age, they should be excluded from the age model.

On the other hand, once the event bed is attributed to Kuwae eruption, it can be incorporated into the depth-age model as a control point. Although the precise dating of Kuwae eruption is controversial, 1450–1458 CE is the acknowledged interval; in this study 1452 CE is adopted as its climactic phase (Robin et al., 1994; Gao et al., 2006; Witter and Self, 2007), and an error of 4 years is assigned exercising caution.

After depth correction, the combined dating results present an almost-perfect chrono-stratigraphy order, yielding an age-depth model back to 3100 yr BP (Fig. 2e) and an almost constant deposition rate (approximately 1 mm/year) in the lagoon. Given the sampling interval of 1 cm, each sample represents approximately 10 years' worth of deposition. The Emau island has undergone minimal agricultural development, and thus the sedimentation rate in the lagoon is considered negligibly influenced by anthropogenic activities.

4.2. Local tropical cyclone variability

4.2.1. TC event bed interpretation

During normal weather, fine grains are transported by tides through the tidal inlet and are accumulated in the Marou Lagoon. The close passage of intense tropical cyclones brings high winds, extreme surface waves, and storm surges. Under such violent dynamic conditions, more marine coarse grains are transported into the lagoon either through the tidal inlet by increased bottom shear stress or in terms of washover and settle down in the deeper part of the lagoon. Due to extreme precipitation during storm landfall, terrigenous fines are transported via sheetwash into the lagoon from the landward side of the lagoon, while only minimal amounts of terrestrial coarse grains reach the sampling site due to the gentle gradient of the landward lakebed, the dense vegetation and thorough weathering on the volcanic cone. Meanwhile, fine-grained benthic sediments on the shallow area of the lagoon undergo resuspension and lateral transportation; due to their slow settling velocity, they mantle the previously deposited coarse grains, forming an event bed.

PAM was rated as one of the most powerful and destructive tropical cyclones on record of Vanuatu (Charan et al., 2017), making direct landfall on the Efate group at category 5 in 2015 (Fig. S2). Hong et al. (2018) investigated PAM-induced deposits from Manuro beach, Efate Island (Fig. 1a). They found the overwash sediment consists of carbonate sands, mollusk and coral fragments, and volcanic sediments, yielding an estimated maximum flow height of 5.29 m mean sea level. It is reasonable to assume comparable dynamic conditions for our site and to infer that the upmost event layer in EMAU with similar coarse contents was induced by PAM. Other Type-II event beds, containing reef-derived coarse grains and pyroclastic sands (Fig. S3), are therefore interpreted as TC deposits given their similarities. This interpretation is also underpinned by comparisons with TC event beds in previous studies from similar sedimentary environments (Toomey et al., 2016; Wallace et al., 2019).

4.2.2. Attribution of modern event beds

Although it has long been challenging to backtrack storm intensity from event deposits due to the complexity of atmospheric-hydraulic-

sediment dynamic processes during a storm event, productive attempts have been made to quantitatively relate event products to TC-induced hydrodynamics under specific sedimentary environments, or to roughly constrain the intensity of causative paleostorms by drawing analogies with modern event deposits (Liu and Fearn, 2000; Elsner et al., 2008; Woodruff et al., 2008; Brandon et al., 2013; Lin et al., 2014; Terry and Lau, 2018; Wallace et al., 2019). The analogy performed by Li et al. (2025) suggests that event beds from a back-reef sinkhole were probably induced by proximal landfalls of intense TCs (category 3 and above on the Saffir-Simpson Hurricane Scale; Taylor et al., 2021), which can serve as a valuable reference considering the similarity between sites.

Due to the presence of dating uncertainties, a more lenient criterion should be adopted when delimiting the scope of modern events. Four visually discernible TC event beds are preserved in the EMAU top section (uncalibrated depth: 0–25 cm), each of which is several centimeters thick. As previously mentioned, resuspension and lateral transportation of fine grains are common under TC-induced dynamic conditions, and their mixing and infilling in TC beds is probably associated with disrupted chronological sequence. Such centimeter-level disturbances would cause complexities in applying the ^{137}Cs and ^{210}Pb dating results, and short-term sedimentation rates that may differ markedly from the overall deposition rate of approximately 1 mm/year. The fact is that these event beds were rapidly deposited with extremely high sedimentation rates during extreme events. However, the specific activity of ^{210}Pb at the top is anomalously low, and the peak of ^{137}Cs occurs at an abnormally shallow depth (Fig. S4), both resulting in deposition rates significantly below average. Such negative deviation would exacerbate (~0.2 mm/year if ^{137}Cs peak is adopted) with depth correction performed. Maintaining a conservative stance, we adopt the radiocarbon-based age model refined with Kuwae event to roughly constrain the age ranges of candidate event beds in the top section of EMAU, and to trace the causative modern TC events.

Instrumental records show that at least 22 tropical cyclones passed within 150 km of the Marou Lagoon since 1963. Amongst them, six were above category 3, whose passage likely instigated hydrodynamic conditions severe enough to leave coarse-grained beds (Fig. S2). The age model dates the upmost event layer between 2006 and 2016 (mean: 2012), supporting the previous attribution to PAM. The second event bed has relatively minor coarse peak than the ones above and below it; it is dated between 1969 and 2013 (mean: 1995) and was most likely generated by the direct landfall of TC IVY (category 3, 2004). Two stacked event beds can be identified by visual inspection from the third major peak in grain size, and their age range from 1930 to 2001 (mean: 1962) and from 1830 to 1995 (mean: 1934), respectively. Concerning that multiple event beds are concentrated in a limited interval, the dating results are probably slightly older than their actual ages, despite depth correction performed. Therefore, we tentatively attribute these two beds to FRAN (category 4, 1992) and PREMA (category 3, 1993).

4.2.3. TC event frequency and variation

Assuming all Type II event beds are related to TCs, the total intense TC number was determined after different cutoff thresholds were performed downcore (Fig. S5). An intense TC event bed was defined as a peak that exceeds the 90th percentile on the cumulative distribution of the coarse anomaly data over the EMAU record. Under this criterion, EMAU has captured 36 intense storm events in the past 3100 years, and the resultant overall average event frequency is approximately 1.2 event per century (Fig. 5c).

TC event frequency was calculated, and this series reveals substantial multi-centennial variability, with active TC occurrence characterizing the twentieth century, 350–750 CE and 1550–1750 CE; in the 1100 years before the common era, only two TC events were captured by EMAU, marking a prominent long quiescent period.

4.3. Climate drivers of intense cyclone variability

4.3.1. Divergent attribution of climatic forcing

Multi-centennial active and quiescent TC activity periods are typically interpreted as climate signals. However, variations in cyclone occurrence within existing prehistorical TC records across the tropical South Pacific exhibit ambiguous and sometimes contradictory attributions, as reviewed below.

Denniston et al. (2015) interpreted the KNI-51 record (Fig. 5a) as a proxy for cyclone-induced extreme rainfall over the past two millennia. They attributed long-term shifts in central Australian cyclogenesis to persistent El Niño or La Niña states in the tropical Pacific. While the study suggests elevated TC activity between the 9th–15th centuries supports a La Niña-like mean state during the medieval period, multi-centennial averages within this interval remain statistically indistinguishable from long-term background levels, questioning the robustness of the 'elevated' designation. Furthermore, the definitive attribution of an El Niño-like state dominating the 16th–19th centuries is compromised by pronounced data scarcity during the 17th–18th centuries and a progressive increase in TC frequency after ~1800 CE.

Toomey et al. (2013) identified two periods of heightened TC activity, 5000–3800 yr BP and 2900–500 yr BP, in a lagoon sediment record from Tahaa, French Polynesia. They argued that ENSO could not fully explain basin-wide synchronicity in TC activity, proposing instead that precession-driven insolation changes steepened ocean-atmosphere thermal gradients, enhancing TC potential intensity in the South Pacific. Their subsequent reconstruction (Toomey et al., 2016) from nearby Apu Bay, Tahaa, features higher TC occurrence between 2600 and 1500 yr BP (650 BCE–450 CE). This interval overlaps with the 2900–500 yr BP window from their 2013 study and resembles trends in contemporary composite beach ridge records from northeastern Australia and KNI-51. They suggest the northward migration and zonal orientation of the SPCZ during this period, modulated by strong ENSO events, created conditions favorable for cyclogenesis near French Polynesia. Notably, while this attribution aligns with short instrumental records (Vincent et al., 2011), it lacks support from long-term SPCZ reconstructions and diverges from their prior work (Toomey et al., 2013), further highlighting contentious interpretations of late Holocene ENSO activity (Cobb et al., 2013).

Li et al. (2025) established a bimillennial cyclone series (BOI; Fig. 5d) using sediment cores from a Fijian sinkhole. Their comparative investigation (including RIDGE and TAHAA records) revealed a basin-wide increase in cyclone frequency during the Little Ice Age (LIA), with its temporal span synchronous with Australasian temperature reconstructions (Fig. 5i; PAGES 2k Consortium, 2013). The BOI record also discloses a quiescent-to-moderate cyclone activity episode during the austral Medieval Climate Anomaly (MCA). Enabled by a multi-millennial SPCZ proxy (Hassall, 2017), they propose that SPCZ displacements modulated by ENSO account for heightened and reduced cyclone occurrence in the LIA and MCA, respectively. However, chronological limitations preclude examination of the Roman Warm Period (RWP), and phases characterized by opposing proxy signals remain unexplored.

4.3.2. Intense cyclone variability driven by SPCZ

The SPCZ extends as a zonal equatorial rainfall band over the Indo-Pacific Warm Pool (IPWP), with a diagonal axis reaching into the subtropical South Pacific (Brown et al., 2020). Instrumental records and climate model outputs have revealed that SPCZ position and structure variations are regulated by ENSO-driven sea surface temperature anomalies (Basher and Zheng, 1995; Cai et al., 2012; Brown et al., 2020). During La Niña events, the diagonal axis shifts ~1°–3° poleward from its climatological position, while moderate El Niño events move it equatorward. During strong El Niño events, the SPCZ diagonal axis can be displaced >10° equatorward by the reorganized tropical Pacific convection and merge with the Intertropical Convergence Zone (ITCZ)
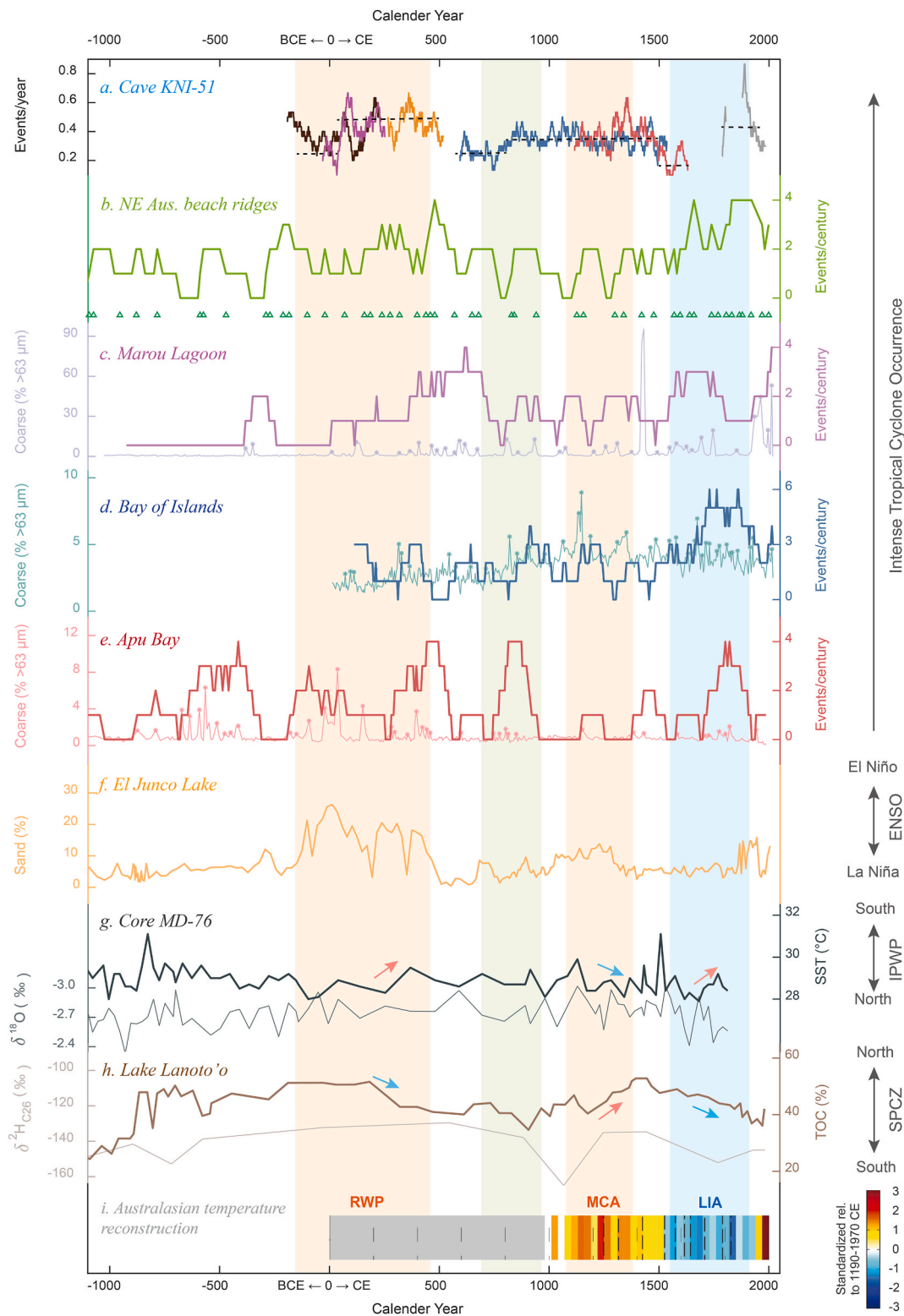
Fig. 5. Paleoclimate and paleostorm reconstructions in the past 3100 years across the South Pacific basin. (a) Flood occurrences (30-year moving mean) reconstructed from KNI-51 stalagmites, with dashed lines representing multi-centennial averages (hereinafter referred to as KNI-51; Denniston et al., 2015). Tropical cyclone occurrences preserved in (b) beach ridges from the northeast Australian coasts (hereinafter referred to as RIDGE; Hayne and Chappell, 2001; Nott et al., 2009; Forsyth et al., 2010; Forsyth et al., 2012) and sediment cores from (c) Marou Lagoon (this study), (d) Bay of Islands, Fiji (hereinafter referred to as BOI; Li et al., 2025) and (e) Apu Bay, Tahaa, French Polynesia (hereinafter referred to as TAHAA; Toomey et al., 2016). (f) Sand contents in a core from El Junco Lake, Galápagos Islands (hereinafter referred to as JUNCO; Conroy et al., 2008). (g) Oxygen isotope and sea surface temperature (SST) derived from the MD982176 (MD-76) marine sediment core (Stott et al., 2004). (h)Total organic carbon (TOC) and δ^2H records retrieved from Lake Lanoto'o, Samoa (hereinafter referred to as LANO; Hassall, 2017). (i) Continental-scaled temperature reconstructions of Australasia, modified from PAGES 2k Consortium (2013). Sites of reconstructions a - h are consecutively numbered 1–8 in Fig. 1a.

into a unified zonal convergence belt over the western-central equatorial Pacific.

Since SPCZ is the main development region (MDR) providing essential conditions favoring cyclogenesis in the South Pacific (Gray, 1979; Jourdain et al., 2011), its spatial and structural variations consequently induce shifts in tropical cyclone genesis locations. However, as established, patterns evident in paleotempestological records often diverge from the SPCZ variations revealed by instrumental observations (Vincent et al., 2011; Dowdy et al., 2012) and climate model outputs (Cai et al., 2012; Evans et al., 2016). This discrepancy arises because a single site provides only fragmentary information that may not represent regional characteristics due to the stochastic nature of cyclogenesis and track. Moreover, each study area possesses a site-specific sensitivity threshold (Elsner et al., 2008), and varying sensitivities to storm activity exacerbate this spatial heterogeneity across sites within the same basin, explaining why previous studies have proposed diverse attributions of climatic drivers. Wallace et al. (2020) contend that randomness—not climatic variability—primarily drives TC frequency variations in Bahamian pseudo-sedimentary records from synthetic storm simulations. They call for caution in inferring basin-scale TC patterns or making claims of climatic drivers on basis of a single record from tropical locales.

It is essential to mitigate the influence of such single sample bias for extracting basin-wide storm activity characteristics over extended timescales, particularly when overall frequencies in storm records are notably low (e.g., 1–2 events/century in EMAU, RIDGE, and TAHAA). The following strategies contribute to this purpose: (1) conducting cross-validation using diverse proxies from multiple sites with a reasonable spatial distribution; (2) focusing on multi-centennial periods of dramatic climate change, wherein climatic signals become more readily extractable; and (3) if possible, enhancing paleotempestological records by extending their temporal coverage while improving temporal resolution.

To diagnose climatic drivers, the three thermal oscillations (RWP, MCA and LIA) constitute the primary focal points. We initially examine the linkage between the SPCZ and ENSO records during the late Holocene using proxy datasets LANO (Fig. 5h; Hassall, 2017) and JUNCO (Fig. 5f; Conroy et al., 2008). LANO reveals a persistent southward displacement of the SPCZ during the LIA, coinciding with La Niña-dominated conditions in that period. While the ENSO phase characterization for the MCA remains debated, LANO indicates that the SPCZ initially fluctuated near its climatological average position in the early MCA, subsequently migrating northward—consistent with prevailing El Niño-like conditions during this interval. Throughout the early-to-mid RWP, the SPCZ resided persistently north of its mean position, corresponding to sustained El Niño-like conditions. By the mid-RWP, however, the SPCZ commenced southward migration toward its average position. This shift occurred despite the overall El Niño-like state, reflecting intermittent intense La Niña events in JUNCO. Notably, the phase relationship after 500 CE shows LANO slightly lagging JUNCO, likely attributable to the delayed onset and end of the MCA and LIA in the Southern Hemisphere (PAGES 2k Consortium, 2013). Collectively, LANO demonstrates strong correspondence with JUNCO during the three warm and cold events.

Integrating the EMAU record, we can perform a comparative analysis consisting of five paleotempestological records derived from multiple proxies across diverse sedimentary environments (Fig. 5). The original datasets (KNI-51 and BOI) from Denniston et al. (2015) and Li et al. (2025) were directly adopted. For comparison, a reprocessed 3000-year storm frequency series following EMAU methodology was added to the original coarse fraction data of Toomey et al. (2016) to generate TAHAA, while a continuous RIDGE sequence was reproduced after Li et al. (2025). Sites of these records are zonally distributed within the narrow strip between 10 and 22°S across the central to western tropical South Pacific, with adjacent sites spaced 1000–2000 km apart (Fig. 1a).

It is intriguing that the patterns identified by Li et al. (2025) across three records (RIDGE, BOI and TAHAA) remains valid with the inclusion of two additional records (KNI-51 and EMAU). Specifically, all five records exhibit enhanced cyclone activity during the LIA, while the temporal offsets in peak occurrence are probably due to the single sampling bias. Conversely, during the MCA, these sites demonstrate relatively quiescent storm activity—at most reaching moderate. During the early RWP (150 BCE–50 CE), storm activity remained quiescent at four sites except for TAHAA, which exhibited heightened activity. In contrast, progressive heightened cyclones occurred across all five sites during the mid-to-late RWP (50–400 CE).

We tend to use a coherent explanatory framework for how the positional and structural variations of SPCZ have modulated cyclogenesis across the South Pacific basin over the past three millennia. The storm activity recorded at RIDGE, EMAU, and BOI corresponds well with shifts in the SPCZ, as these sites fall under the western flank of the SPCZ diagonal axis under climatological average conditions. Consequently, SPCZ migration directly influences cyclone occurrence in their vicinity, consistent with instrumental records. However, the KNI-51 and TAHAA records warrant particular attention in the subsequent discussion since they exhibit distinctive features. First, the KNI-51 record, previously interpreted as reflecting ENSO variability or serving as an ITCZ indicator, exhibits a pattern remarkably similar to the first three records (especially RIDGE), despite its considerable distance from the SPCZ diagonal band. Secondly, the TAHAA record, situated near the SPCZ diagonal axis, displays a see-saw pattern with RIDGE and EMAU–attributable to SPCZ migration as revealed by instrumental records – only during the early RWP. During the mid-late RWP, MCA and LIA, its pattern aligns closely with the other records.

During periods of frequent strong La Niña events (e.g., LIA, late RWP), the SPCZ diagonal band not only shifted southwestward but also underwent lateral expansion. Concurrently, the zonal branch of the SPCZ extended southward due to the accumulation of warm water and expansion of the IPWP (Brown et al., 2020, Fig. 3), enveloping all five sites within the MDR. Furthermore, enhanced overall tropical cyclone genesis frequency across the equatorial Pacific, driven by atmospheric circulation changes (Bramante et al., 2020), resulted in increased storm activity observed in all records.

Conversely, under persistent, strong El Niño-like conditions (e.g., early RWP), the IPWP contracted due to weakened trade winds and reduced warm water supply, causing the SPCZ diagonal band to shift equatorward and collapse into a zonal structure. Consequently, the main body of the SPCZ, located north of French Polynesia (Toomey et al., 2016; Brown et al., 2020), generated most South Pacific storms, leading to enhanced storm activity recorded at TAHAA. In contrast, the RIDGE, EMAU, and BOI sites, now situated far from the SPCZ, experienced relatively quiescent storm activity. Simultaneously, reduced storm genesis occurred over the contracted Warm Pool, and the thermal conditions in the Arafura Sea (MD-76; Fig. 5g) north of Cave KNI-51 became less favorable for storm development.

Under weak-to-moderate El Niño-like conditions (e.g., MCA), stochastic factors began to dominate, as suggested by Wallace et al. (2020). Moreover, the overall tropical cyclone frequency likely exhibited no significant change, explaining the moderate-to-quiet levels of storm activity observed in all records during this interval. Similarly, the see-saw pattern observed during 400–900 CE, reflects the dominance of this stochastic rather than climatical signal.

5. Conclusions

This study establishes a 3100-year record of intense tropical cyclone (TC) activity in the central South Pacific using sediments from Marou Lagoon, Emau Island, Vanuatu (EMAU core). With coarse anomalies used as the main proxy and integration of modern analogs (e.g., Cyclone Pam, 2015), 36 intense tropical cyclones (Categories ≥3) are identified, yielding a mean frequency of ~1.2 events/century. Pronounced multi-centennial variability features active phases during the Little Ice Age

(1550–1750 CE), 350–750 CE, and the 20th century, contrasting with a 1100-year quiescent period pre-dating the Common Era.

Synchronized examination of five paleotempestological records (RIDGE, BOI, TAHAA, KNI-51, EMAU) demonstrates that multidecadal-to-centennial tropical cyclone variability across the South Pacific is dominantly governed by ENSO-driven shifts in the South Pacific Convergence Zone (SPCZ). During La Niña-dominated periods (e.g., Little Ice Age, late Roman Warm Period), the SPCZ diagonal axis shifted southwestward and underwent lateral expansion while its zonal branch extended southward due to Indo-Pacific Warm Pool expansion. This configuration enveloped all five sites within the main development region, enhancing cyclone genesis frequency basin-wide. Conversely, under persistent strong El Niño-like conditions (e.g., early Roman Warm Period), SPCZ collapse into a contracted zonal structure near French Polynesia concentrated storm activity at eastern sites (notably TAHAA) while suppressing the others in western locations—explaining the observed early-RWP see-saw pattern. During weak-to-moderate El Niño-like states (e.g., MCA), stochastic factors override climatic drivers, explaining moderate-to-low TC activity across all records. Critically, storm signals across all sites during climatically extreme intervals validate SPCZ reorganization as the principal mechanism synchronizing basin-wide TC activity over the past three millennia.

Sedimentological evidence (complex composition, sorting, and cyclic structures) confirms the most conspicuous event bed at Emau Island records a tsunami event, not a tropical cyclone. Chronological constraints robustly link this deposit to the cataclysmic mid-15th century Kuwae eruption. The tsunami deposit exhibits a five-stage sequence (SL1–SL5) reflecting the eruption's progression and providing unprecedented resolution of eruption dynamics and tsunami impacts, surpassing subaerial records.

Sheltering by the lagoon barrier and reef, combined with water depth, precluded hummocky cross-stratification and bidirectional flow structures—features typically diagnostic of tsunami deposits. Furthermore, the heterogeneous density and shape of pyroclastic material (especially pumice) invalidate standard grain-size-based hydraulic models, underscoring the need for lithology-specific dynamic modeling in volcanic-coral reef settings.

This study demonstrates that sheltered tropical lagoons can preserve high-fidelity, records of both extreme cyclones and volcanogenic multistage tsunamis. Such records offer critical insights into regional climatic drivers and geohazard mechanisms but necessitate environment-specific sedimentological frameworks, particularly where low-density pyroclastics dominate coarse fractions.

Declaration of competing interest

The authors declare that they have no known competing financial interests or personal relationships that could have appeared to influence the work reported in this paper.

Acknowledgement

Appendix A. Supplementary data

Supplementary data to this article can be found online at https://doi. org/10.1016/j.quascirev.2025.109733.

Data availability

All data and/or code is contained within the submission.

References

Basher, R.E., Zheng, X., 1995. Tropical cyclones in the Southwest Pacific: spatial patterns and relationships to Southern oscillation and Sea surface temperature. J. Clim. 8 (5), 1249–1260. https://doi.org/10.1175/1520-0442(1995)008<1249:TCITSP>2.0.CO;2.

Biguenet, M., Chaumillon, E., Sabatier, P., Paris, R., Vacher, P., Feuillet, N., 2022. Discriminating between tsunamis and tropical cyclones in the sedimentary record using X-ray tomography. Mar. Geol. 450. https://doi.org/10.1016/j.margeo.2022.106864.

Blaauw, M., Christen, J.A., 2011. Flexible paleoclimate age-depth models using an autoregressive gamma process. Bayesian Anal. 6 (3), 457–474. https://doi.org/10.1214/11-BA618.

Bramante, J.F., Ford, M.R., Kench, P.S., Ashton, A.D., Toomey, M.R., Sullivan, R.M., et al., 2020. Increased typhoon activity in the Pacific deep tropics driven by little Ice Age circulation changes. Nat. Geosci. 13 (12), 806–811. https://doi.org/10.1038/s41561-020-00656-2.

Brandon, C.M., Woodruff, J.D., Lane, D., Donnelly, J.P., 2013. Tropical cyclone wind speed constraints from resultant storm surge deposition: a 2500 year reconstruction of hurricane activity from st. Marks, FL. G-cubed 14 (8), 2993–3008. https://doi.org/10.1002/ggge.20217.

Briffa, K.R., Jones, P.D., Schweingruber, F.H., Osborn, T.J., 1998. Influence of volcanic eruptions on Northern Hemisphere summer temperature over the past 600 years. Nature 393 (6684), 450–455. https://doi.org/10.1038/30943.

Brown, J.R., Lengaigne, M., Lintner, B.R., Widlansky, M.J., van der Wiel, K., Dutheil, C., et al., 2020. South Pacific convergence zone dynamics, variability and impacts in a changing climate. Nat. Rev. Earth Environ. 1 (10), 530–543. https://doi.org/10.1038/s43017-020-0078-2.

Bureau of Meteorology, Australia Government, 2024. Tide predictions for Australia, South Pacific and Antarctica. URL. http://www.bom.gov.au/australia/tides/#!/offshore. (Accessed 12 October 2024).

Cai, W., Lengaigne, M., Borlace, S., Collins, M., Cowan, T., McPhaden, M.J., et al., 2012. More extreme swings of the South Pacific convergence zone due to greenhouse warming. Nature 488 (7411), 365–369. https://doi.org/10.1038/nature11358.

Charan, D., Kaur, M., Singh, P., 2017. Customary land and climate change induced relocation—A case study of vunidogoloa village, Vanua Levu, Fiji. In: Leal Filho, W. (Ed.), Climate Change Adaptation in Pacific Countries: Fostering Resilience and Improving the Quality of Life. Springer International Publishing, Cham, pp. 19–33.

Cobb, K.M., Westphal, N., Sayani, H.R., Watson, J.T., Di Lorenzo, E., Cheng, H., et al., 2013. Highly variable El niño–southern oscillation throughout the Holocene. Science 339 (6115), 67–70. https://doi.org/10.1126/science.1228246.

Conroy, J.L., Overpeck, J.T., Cole, J.E., Shanahan, T.M., Steinitz-Kannan, M., 2008. Holocene changes in eastern tropical Pacific climate inferred from a Galápagos lake sediment record. Quat. Sci. Rev. 27 (11), 1166–1180. https://doi.org/10.1016/j.quascirev.2008.02.015.

Day, S.J., 2015. Chapter 58 - volcanic tsunamis. In: Sigurdsson, H. (Ed.), The Encyclopedia of Volcanoes, second ed. Academic Press, Amsterdam, pp. 993–1009.

Denniston, R.F., Villarini, G., Gonzales, A.N., Wyrwoll, K.-H., Polyak, V.J., Ummenhofer, C.C., et al., 2015. Extreme rainfall activity in the Australian tropics reflects changes in the El Niño/Southern Oscillation over the last two millennia. Proc. Natl. Acad. Sci. 112 (15), 4576–4581. https://doi.org/10.1073/pnas.1422270112.

Dean, W.E., 1974. Determination of carbonate and organic matter in calcareous sediments and sedimentary rocks by loss on ignition; comparison with other methods. J. Sediment. Res. 44 (1), 242–248. https://doi.org/10.1306/74D729C0-2B21-11D7-8648000102C1865D.

Dioguardi, F., Mele, D., Dellino, P., 2018. A new one-equation model of fluid drag for irregularly shaped particles valid over a wide range of Reynolds number. J. Geophys. Res. Solid Earth 123 (1), 144–156. https://doi.org/10.1002/2017JB014927.

Donato, S.V., Reinhardt, E.G., Boyce, J.I., Pilarczyk, J.E., Jupp, B.P., 2009. Particle-size distribution of inferred tsunami deposits in Sur Lagoon, Sultanate of Oman. Mar. Geol. 257 (1), 54–64. https://doi.org/10.1016/j.margeo.2008.10.009.

Donnelly, J.P., Roll, S., Wengren, M., Butler, J., Lederer, R., Webb Iii, T., 2001. Sedimentary evidence of intense hurricane strikes from New Jersey. Geology 29 (7), 615–618. https://doi.org/10.1130/0091-7613(2001)029<0615:SEOISH>2.0.CO;2.

Donnelly, J.P., Woodruff, J.D., 2007. Intense hurricane activity over the past 5,000 years controlled by El Niño and the West African monsoon. Nature 447 (7143), 465. https://doi.org/10.1038/nature05895.

Donnelly, J.P., Hawkes, A.D., Lane, P., MacDonald, D., Shuman, B.N., Toomey, M.R., et al., 2015. Climate forcing of unprecedented intense-hurricane activity in the last 2000 years. Earths Future 3 (2), 49–65. https://doi.org/10.1002/2014EF000274.

Donnelly, J.P., 2025. Reconstructing tropical cyclone activity from sedimentary archives. Annu. Rev. Earth Planet Sci. 53 (53), 251–281. https://doi.org/10.1146/annurev-earth-040522-113454.

Dott Jr., R.H., Bourgeois, J., 1982. Hummocky stratification: significance of its variable bedding sequences. GSA Bull. 93 (8), 663–680. https://doi.org/10.1130/0016-7606(1982)93<663:HSSOIV>2.0.CO;2.

Dowdy, A.J., Qi, L., Jones, D., Ramsay, H., Fawcett, R., Kuleshov, Y., 2012. Tropical cyclone climatology of the South Pacific Ocean and its relationship to El niño–southern oscillation. J. Clim. 25 (18), 6108–6122. https://doi.org/10.1175/JCLI-D-11-00678.1.

Elsner, J.B., Jagger, T.H., Liu, K.-b., 2008. Comparison of hurricane return levels using historical and geological records. J. Appl. Meteorol. Climatol. 47 (2), 368–374. https://doi.org/10.1175/2007JAMC1692.1.

Emery, K.O., 1969. A Coastal Pond Studied by Oceanographic Methods. Elsevier, New York, p. 82.

Evans, J.P., Bormann, K., Katzfey, J., Dean, S., Arritt, R., 2016. Regional climate model projections of the South Pacific convergence zone. Clim. Dyn. 47 (3), 817–829. https://doi.org/10.1007/s00382-015-2873-x.

Forsyth, A.J., Nott, J., Bateman, M.D., 2010. Beach ridge plain evidence of a variable late-holocene tropical cyclone climate, North Queensland, Australia. Palaeogeogr. Palaeoclimatol. Palaeoecol. 297 (3), 707–716. https://doi.org/10.1016/j.palaeo.2010.09.021.

Forsyth, A.J., Nott, J., Bateman, M.D., Beaman, R.J., 2012. Juxtaposed beach ridges and foredunes within a ridge plain — wonga beach, northeast Australia. Mar. Geol. 307–310, 111–116. https://doi.org/10.1016/j.margeo.2012.03.006.

Fujino, S., Masuda, F., Tagomori, S., Matsumoto, D., 2006. Structure and depositional processes of a gravelly tsunami deposit in a shallow marine setting: Lower Cretaceous Miyako Group, Japan. Sediment. Geol. 187 (3), 127–138. https://doi.org/10.1016/j.sedgeo.2006.01.009.

Fujiwara, O., Masuda, F., Sakai, T., Irizuki, T., Fuse, K., 2000. Tsunami deposits in Holocene bay mud in southern Kanto region, Pacific coast of central Japan. Sediment. Geol. 135 (1), 219–230. https://doi.org/10.1016/S0037-0738(00)00069-1.

Fujiwara, O., Kamataki, T., 2007. Identification of tsunami deposits considering the tsunami waveform: an example of subaqueous tsunami deposits in Holocene shallow bay on southern Boso Peninsula, Central Japan. Sediment. Geol. 200 (3–4), 295–313. https://doi.org/10.1016/j.sedgeo.2007.01.015.

Gao, C., Robock, A., Self, S., Witter, J.B., Steffenson, J.P., Clausen, H.B., et al., 2006. The 1452 or 1453 A.D. Kuwae eruption signal derived from multiple ice core records: greatest volcanic sulfate event of the past 700 years. J. Geophys. Res. Atmos. 111 (D12). https://doi.org/10.1029/2005JD006710.

Garanger, J., 1972. Archéologie Des Nouvelles-Hébrides: Contribution à la connaissance des îles du centre. Paris: Société des Océanistes.

Goff, J., Charley, D., Haruel, C., Bonte-grapetntin, M., 2008. Preliminary Findings of the Geological Evidence and Oral History of Tsunamis in Vanuatu, Pacific Islands. Retrieved from Suva, Fiji Islands.

Goff, J., Chagué-Goff, C., Dominey-Howes, D., McAdoo, B., Cronin, S., Bonté-Grapetin, M., et al., 2011. Palaeotsunamis in the Pacific Islands. Earth Sci. Rev. 107 (1–2), 141–146. https://doi.org/10.1016/j.earscirev.2011.01.005.

Gray, W.M., 1979. Hurricanes: their formation, structure and likely role in the tropical circulation. Meteorology over the Tropical Oceans, pp. 155–218.

Hassall, J.D., 2017. Static or Dynamic: Reconstructing past Movement of the South Pacific Convergence Zone. University of Southampton.

Hayne, M., Chappell, J., 2001. Cyclone frequency during the last 5000 years at Curacoa Island, north Queensland, Australia. Palaeogeogr. Palaeoclimatol. Palaeoecol. 168 (3), 207–219. https://doi.org/10.1016/S0031-0182(01)00204-5.

Hong, I., Pilarczyk, J.E., Horton, B.P., Fritz, H.M., Kosciuch, T.J., Wallace, D.J., et al., 2018. Sedimentological characteristics of the 2015 tropical cyclone pam overwash sediments from Vanuatu, South Pacific. Mar. Geol. 396, 205–214. https://doi.org/10.1016/j.margeo.2017.08.014.

Jaffe, B.E., Gelfenbuam, G., 2007. A simple model for calculating tsunami flow speed from tsunami deposits. Sediment. Geol. 200 (3), 347–361. https://doi.org/10.1016/j.sedgeo.2007.01.013.

Jourdain, N.C., Marchesiello, P., Menkes, C.E., Lefèvre, J., Vincent, E.M., Lengaigne, M., Chauvin, F., 2011. Mesoscale simulation of tropical cyclones in the South Pacific: climatology and interannual variability. J. Clim. 24 (1), 3–25. https://doi.org/10.1175/2010JCLI3687.1.

Kruger-Knuepfer, J.L., Chatelain, J., Hamburger, M.W., Isacks, B.L., Barazangi, M., Hade, G., et al., 1986. Evaluation of seismic risk in the Tonga-Fiji-Vanuatu region of the southwest Pacific: a country report: republic of Vanuatu. Retrieved from. https://core.ac.uk/download/pdf/39871021.pdf.

Lane, P., Donnelly, J.P., Woodruff, J.D., Hawkes, A.D., 2011. A decadally-resolved paleohurricane record archived in the late Holocene sediments of a Florida sinkhole. Mar. Geol. 287 (1–4), 14–30. https://doi.org/10.1016/j.margeo.2011.07.004.

Li, Y., Donnelly, J.P., d'Entremont, N., Bramante, J.F., Kotra, K.K., Gao, S., 2025. Intense tropical cyclone activity over the past 2000 years at Bay of Islands, Fiji. Palaeogeogr. Palaeoclimatol. Palaeoecol. 675, 113090. https://doi.org/10.1016/j.palaeo.2024.113090.

Lin, N., Lane, P., Emanuel, K.A., Sullivan, R.M., Donnelly, J.P., 2014. Heightened hurricane surge risk in northwest Florida revealed from climatological-hydrodynamic modeling and paleorecord reconstruction. J. Geophys. Res. Atmos. 119 (14), 8606–8623. https://doi.org/10.1002/2013JD021367.

Liu, K.-b., Fearn, M.L., 2000. Reconstruction of prehistoric landfall frequencies of catastrophic hurricanes in northwestern Florida from lake sediment records. Quat. Res. 54 (2), 238–245. https://doi.org/10.1006/qres.2000.2166.

Liu, K.-b., Shen, C., Louie, K.-s., 2001. A 1,000-Year history of typhoon landfalls in Guangdong, Southern China, reconstructed from Chinese historical documentary records. Ann. Assoc. Am. Geogr. 91 (3), 453–464. https://doi.org/10.1111/0004-5608.00253.

Moreira, S., Costa, P.J.M., Andrade, C., Ponte Lira, C., Freitas, M.C., Oliveira, M.A., Reichart, G.-J., 2017. High resolution geochemical and grain-size analysis of the AD 1755 tsunami deposit: insights into the inland extent and inundation phases. Mar. Geol. 390, 94–105. https://doi.org/10.1016/j.margeo.2017.06.004.

Nott, J., Smithers, S., Walsh, K., Rhodes, E., 2009. Sand beach ridges record 6000 year history of extreme tropical cyclone activity in northeastern Australia. Quat. Sci. Rev. 28 (15–16), 1511–1520. https://doi.org/10.1016/j.quascirev.2009.02.014.

PACCSAP, 2015. Current and future climate of the Vanuatu. Retrieved from. https://www.pacificclimatechangescience.org/wp-content/uploads/2013/06/15_PACCSAP-Vanuatu-11pp_WEB.pdf.

PAGES 2k Consortium, 2013. Continental-scale temperature variability during the past two millennia. Nat. Geosci. 6 (5), 339–346. https://doi.org/10.1038/ngeo1797.

Paris, R., Switzer, A.D., Belousova, M., Belousov, A., Ontowirjo, B., Whelley, P.L., Ulvrova, M., 2014. Volcanic tsunami: a review of source mechanisms, past events and hazards in Southeast Asia (Indonesia, Philippines, Papua New Guinea). Nat. Hazards 70 (1), 447–470. https://doi.org/10.1007/s11069-013-0822-8.

Raos, A.M., 2001. The volcanic and geochemical evolution of a trachydacite-dominated island arc centre. Efaté Island Group, Vanuatu Arc, SW Pacific. University of Tasmania.

Robin, C., Monzier, M., Eissen, J.-P., 1994. Formation of the mid-fifteenth century Kuwae caldera (Vanuatu) by an initial hydroclastic and subsequent ignimbritic eruption. Bull. Volcanol. 56 (3), 170–183. https://doi.org/10.1007/BF00279606.

Ruehr, S., 2021. Beyond the Vulnerability/resilience dichotomy: perceptions of and responses to the climate crisis on emau, Vanuatu. Island Stud. J. 17. https://doi.org/10.24043/isj.176.

Spiske, M., Piepenbreier, J., Benavente, C., Bahlburg, H., 2013. Preservation potential of tsunami deposits on arid siliciclastic coasts. Earth Sci. Rev. 126, 58–73. https://doi.org/10.1016/j.earscirev.2013.07.009.

Stott, L., Cannariato, K., Thunell, R., Haug, G.H., Koutavas, A., Lund, S., 2004. Decline of surface temperature and salinity in the western tropical Pacific Ocean in the Holocene epoch. Nature 431 (7004), 56–59. https://doi.org/10.1038/nature02903.

Tan, F., Zhang, Y., Cao, L., Xu, H., Shi, Q., Zhang, X., et al., 2023. Meridional response of Western North Pacific paleocyclone activity to tropical atmospheric circulation variability over the past millennium. Palaeogeogr. Palaeoclimatol. Palaeoecol. 610. https://doi.org/10.1016/j.palaeo.2022.111331.

Taylor, H.T., Ward, B., Willis, M., Zaleski, W., 2021. The Saffir-Simpson hurricane wind scale. Retrieved from. https://www.nhc.noaa.gov/pdf/sshws.pdf.

Terry, J.P., Lau, A.Y.A., 2018. Magnitudes of nearshore waves generated by tropical cyclone Winston, the strongest landfalling cyclone in South Pacific records. Unprecedented or unremarkable? Sediment. Geol. 364, 276–285. https://doi.org/10.1016/j.sedgeo.2017.12.018.

Terry, J.P., Goff, J., Winspear, N., Bongolan, V.P., Fisher, S., 2022. Tonga volcanic eruption and tsunami, January 2022: globally the most significant opportunity to observe an explosive and tsunamigenic submarine eruption since AD 1883 Krakatau. Geosci. Lett. 9 (1), 24. https://doi.org/10.1186/s40562-022-00232-z.

Toomey, M.R., Curry, W.B., Donnelly, J.P., van Hengstum, P.J., 2013. Reconstructing 7000 years of North Atlantic hurricane variability using deep-sea sediment cores from the western Great Bahama Bank. Paleoceanography 28 (1), 31–41. https://doi.org/10.1002/palo.20012.

Toomey, M.R., Donnelly, J.P., Tierney, J.E., 2016. South Pacific hydrologic and cyclone variability during the last 3000 years. Paleoceanography 31 (4), 491–504. https://doi.org/10.1002/2015PA002901.

Vincent, E.M., Lengaigne, M., Menkes, C.E., Jourdain, N.C., Marchesiello, P., Madec, G., 2011. Interannual variability of the South Pacific Convergence Zone and implications for tropical cyclone genesis. Clim. Dyn. 36 (9), 1881–1896. https://doi.org/10.1007/s00382-010-0906-z.

Wallace, E.J., Coats, S., Emanuel, K.A., Donnelly, J.P., 2020. Centennial-scale shifts in storm frequency in paleohurricane records from The Bahamas arise predominantly from random variability. Geophys. Res. Lett. 48 (1). https://doi.org/10.1029/2020GL091145.

Wallace, E.J., Donnelly, J.P., van Hengstum, P.J., Wiman, C., Sullivan, R.M., Winkler, T. S., et al., 2019. Intense hurricane activity over the past 1500 years at South Andros Island, The Bahamas. Paleoceanogr. 36 (11), 1761–1783. https://doi.org/10.1029/2019PA003665.

Witter, J.B., Self, S., 2007. The Kuwae (Vanuatu) eruption of AD 1452: potential magnitude and volatile release. Bull. Volcanol. 69 (3), 301–318. https://doi.org/10.1007/s00445-006-0075-4.

Woodruff, J.D., Donnelly, J.P., Mohrig, D., Geyer, W.R., 2008. Reconstructing relative flooding intensities responsible for hurricane-induced deposits from Laguna Playa Grande, Vieques, Puerto Rico. Geology 36 (5), 391–394. https://doi.org/10.1130/G24731A.1.

Woods, A.W., 1995. The dynamics of explosive volcanic eruptions. Rev. Geophys. 33 (4), 495–530. https://doi.org/10.1029/95RG02096.

Yang, Y., Piper, D.J.W., Xu, M., Gao, J., Jia, J., Normandeau, A., et al., 2022. Northwestern Pacific tropical cyclone activity enhanced by increased Asian dust emissions during the Little Ice Age. Nat. Commun. 13 (1), 1712. https://doi.org/10.1038/s41467-022-29386-2.

Yu, K.-F., Zhao, J.-X., Shi, Q., Meng, Q.-S., 2009. Reconstruction of storm/tsunami records over the last 4000 years using transported coral blocks and lagoon sediments in the southern South China Sea. Quat. Int. 195 (1–2), 128–137. https://doi.org/10.1016/j.quaint.2008.05.023.

Yue, Y., Yu, K., Tao, S., Zhang, H., Liu, G., Wang, N., et al., 2019. 3500-year western Pacific storm record warns of additional storm activity in a warming warm pool. Palaeogeogr. Palaeoclimatol. Palaeoecol. 521, 57–71. https://doi.org/10.1016/j.palaeo.2019.02.011.